

This is the accepted version of the following article

Roman Svoboda, Daniela Brandová (2019). Crystallization behavior of $(\text{GeTe}_4)_x(\text{GaTe}_3)_{100-x}$ glasses for far-infrared optics applications. *Journal of Alloys and Compounds*. DOI: 10.1016/j.jallcom.2018.08.150

This accepted version is available from URI <https://hdl.handle.net/10195/74730>

Publisher's version is available from:

<https://www.sciencedirect.com/science/article/pii/S0925838818330305?via%3Dihub>



This version is licenced under a [Creative Commons Attribution-NonCommercial-NoDerivatives 4.0 International](https://creativecommons.org/licenses/by-nc-nd/4.0/).

Crystallization behavior of $(\text{GeTe}_4)_x(\text{GaTe}_3)_{100-x}$ glasses for far-infrared optics applications

Roman Svoboda^{*1}, Daniela Brandová¹

¹*Department of Physical Chemistry, Faculty of Chemical Technology, University of Pardubice, Studentská 573, 532 10 Pardubice, Czech Republic.*

Abstract

Differential scanning calorimetry (DSC), X-ray diffraction (XRD), infrared microscopy and Raman spectroscopy were used to study the crystallization behavior of the $(\text{GeTe}_4)_x(\text{GaTe}_3)_{100-x}$ glasses for far-infrared optics. Two independent overlapping crystallization processes were found – the initial surface-located precipitation of hexagonal Te and Ga_2Te_5 phases, followed by formation of the rhombohedral GeTe phase. The initial precipitation process, and in particular the formation of the Ga_2Te_5 phase, was found to be catalyzed by presence of mechanically induced defects. Finely powdered materials with higher GaTe_3 content also exhibited more pronounced separation of the two crystallization sub-processes. Glass stability of the prepared glasses was evaluated in terms of the Hrubý criterion - the $(\text{GeTe}_4)_{86}(\text{GaTe}_3)_{14}$ composition was found to be the most stable and most resilient to the negative crystallization-enhancing influence of structure defects. Pros and cons of the compositional evolution of the crystallization behaviour (determined via full kinetic description of the involved crystallization sub-processes and kinetic prediction of the crystallization behavior) were discussed with regard to the ceramics and glass-ceramics applications. Glasses with low GaTe_3 content appear to be most suitable for preparation of fully ceramic materials, whereas glasses with high GaTe_3 content seem to be most suitable for the glass-ceramics applications.

Keywords: Ge-Ga-Te glasses; crystallization kinetics; DSC; XRD; glass-ceramics

* Corresponding author: Tel.: +420 466 037 346 E-mail address: roman.svoboda@upce.cz

1. Introduction

Fully telluride chalcogenides based on the GeTe_4 alloy belong among the most promising materials for far-infrared optics applications (with the only real competition being the $(\text{As}_2\text{Se}_3)_x(\text{As}_2\text{Te}_3)_{100-x}$ glasses). [1, 2] The benefit of fully telluride GeTe_4 matrix (its high transmittance in the far-infrared (IR) region reaching up to $\sim 28 \mu\text{m}$ [3]) is counterbalanced by the GeTe_4 material being a poor glass-former, certainly not sufficient for e.g. fiber-drawing or lens-moulding applications. [4, 5] This issue can be solved by addition of a glass-forming element - the most common choices include Se, Ga and I. [6 - 9] As selenium and iodine exhibit certain disadvantages (addition of selenium narrows the transmittance window; volatility of iodine complicates the synthesis and may lead its non-homogeneous distribution in the base matrix), addition of gallium appears to be most suitable. Suitability of the Ge-Ga-Te chalcogenide system for the far-infrared optics applications was from the optical point of view (high transmittance up to $28 \mu\text{m}$ confirmed in [6, 10, 11], however only very little is known about the thermal properties of these glasses. The glass-forming region in the Ge-Ga-Te chalcogenide system is centred along the pseudo-binary $\text{GeTe}_4\text{-GaTe}_3$ line as reported in [6]. The contemporary literature on Ge-Ga-Te chalcogenide glasses contains only very few information about the thermal properties of these materials, majority of the articles reports only the characteristic temperatures corresponding to glass transition T_g , crystallization peak T_c and melting onset T_m . [6, 10 - 12]

Detailed knowledge of the thermal behavior and crystallization kinetics in particular is important not only for safe processing of the prepared glassy material (e.g. the fiber-drawing or lens-moulding procedures) but it is also crucial for preparation of the corresponding glass-ceramics with enhanced mechanical properties, which are determined by the fraction of the crystalline phase and by the quality of the formed crystallites. [13, 14] Note that the chalcogenide glass ceramics is readily used in various fields [15 - 19], potential applicability

of the $(\text{GeTe}_2)_{80}(\text{Ga}_2\text{Te}_3)_{20}$ ceramics for thermoelectric applications and PCRAM data-storage was suggested in [20]. The Ge-Ga-Te glass-ceramics with its enhanced mechanical properties and good far-IR transparency could then find usage in applications demanding high performance under extreme conditions (e.g. in construction of space telescopes searching for the traces of CO_2 , O_3 and H_2O as signs of extra-terrestrial life [6, 10 - 12]).

In the present article a detailed study of thermally induced crystal formation in the $(\text{GeTe}_4)_x(\text{GaTe}_3)_{100-x}$ chalcogenide glasses will be reported. The kinetics of crystallization in these materials will be described in dependence on particle size of the powdered glass to account for different routes of synthesis and potential applications. The predicative potential of the performed kinetic calculations will be critically discussed with regard to the preparation of Ge-Ga-Te glass-ceramics.

2. Experimental

The $(\text{GeTe}_4)_x(\text{GaTe}_3)_{100-x}$ glasses (for $x = 40, 50, 60, 67, 75, 86$ and 100) were prepared by the common melt-quenching technique; adequate amount of pure elements (5N Sigma-Aldrich) were introduced in fused silica ampoules, which were consequently evacuated, sealed and annealed at $950\text{ }^\circ\text{C}$ for 24 h (followed by water-quenching). The prepared glassy ingots were powdered (using agate mortar and pestle) and sieved through sieves with defined mesh size to obtain the following particle size fractions: 20–50, 125–180 and 300–500 μm .

The thermally induced crystallization was studied by means of differential scanning calorimetry, using the Q2000 heat-flow DSC device (TA Instruments) equipped with an autosampler, RCS90 cooling accessory, and T-zero technology. The instrument was calibrated using In, Zn, and H_2O ; dry N_2 was used as purge gas at a flow rate of $50\text{ cm}^3\cdot\text{min}^{-1}$. The sample controlled to be 8–10 mg was weighed into an aluminum pan and hermetically

sealed. The DSC measurements were performed as simple heating scans between 150 and 450 °C; the following heating rates q^+ were applied for each particle size fraction: 0.5, 1, 2, 5, 10 and 20 °C·min⁻¹. Very good reproducibility of the experimental data was achieved – both position and shape of the kinetic peaks were exactly similar for 20 measurements selected across the matrix of experimental/compositional conditions.

The XRD analysis of amorphous and crystalline samples was performed using a Bruker AXS diffractometer D8 Advance equipped with a horizontal goniometer and scintillation counter utilizing CuK_α radiation. Fully amorphous character of the as-prepared glasses was confirmed. It was also verified that the grinding procedure applied to obtain different powder size fractions did not cause any crystallization. The crystallization products were examined also by means of the infrared microscope Olympus BX51 equipped with XM10 camera (reflection mode). Structural information was obtained by the Nicolet DXR Raman spectrometer (Thermo Fisher Scientific) utilizing 780 nm excitation laser (10 mW, 200 scans → 10 s each) with laser spot size equal to 3.1 μm. Compositional homogeneity of the as-prepared Ge-Ga-Te glasses was confirmed by measurements of the glass transition effect for samples taken randomly from the as-prepared glassy ingot taken out of the ampoule – both position and height of the relaxation peak matched perfectly; no shoulders or double-peak effects occurred.

3. Results and discussion

Typical DSC records corresponding to the measurements performed for 125–180 μm powders at 1 °C·min⁻¹ are for all studied (GeTe₄)_x(GaTe₃)_{100-x} compositions depicted in Fig. 1A. The crystallization effects show a very consistent trend with decrease of GeTe₄ content – the shape-wise almost uniform single peak (exhibiting only minuscule shoulder) present for pure GeTe₄ gets split into two sub-peaks: the first sub-peak having the same

original onset and the second sub-peak being gradually shift to higher temperatures with increasing GaTe₃ content. Akin behaviour was previously reported for the Se-doped GeTe₄ glasses, where the first (low-temperature) peak corresponded to the surface precipitation of hexagonal Te and the second (high-temperature) crystallization peak corresponded to formation of rhombohedral GeTe phase and additional unidentified Ge-Te-Se phases. [21 - 23] Based on the evolution of the shape of melting peaks, the system clearly exhibits eutectic at ~ 357 °C; the exact eutectic composition appears to be very close to (GeTe₄)_{66.6}(GaTe₃)_{33.3}; i.e. possibly lying directly on the presently studied compositional line. Note that the depicted DSC curves are truly representative as only negligible changes in the shape of crystallization and melting peaks occurred with changing heating rate.

The base structural information was for the prepared (GeTe₄)_x(GaTe₃)_{100-x} glasses obtained by Raman spectroscopy – the spectra are depicted in Fig. 1B. The Raman peaks can be assigned as follows: peak at 106 cm⁻¹ corresponds to the corner-shared GeTe₄ tetrahedra and vibrations of the defective octahedral environment in the GeTe₄ tetrahedra. [24 - 26]; peak at 125 cm⁻¹ corresponds to the symmetric stretching mode of corner-sharing Te-rich GeTe_{4-n}Ge_n (n = 0, 1, 2) tetrahedra [24, 27, 28]; peak at 140 cm⁻¹ corresponds to highly ordered Te structures [27, 29, 30]; and peak at 154 cm⁻¹ corresponds to symmetric stretching mode of edge-sharing GeTe₄ (or Ge-rich) tetrahedra, and to a contribution from short, amorphous, distorted Te chains [24, 26, 28, 31]. There is still some uncertainty about the exact bonding arrangements of Ga in the Ge-Ga-Te glasses: [32] reports gallium to be 3-fold coordinated and forming covalent bonds with non-bonding p electrons of Te, i.e. Ga atoms do not build into the Ge-Te covalent network; on the other hand in [33] gallium was reported to be 4-fold coordinated and built directly into the Ge-Ga-Te tetrahedral network. The assignment of the Ga-Te Raman vibrations is therefore still associated with uncertainty. It is reported in [25, 33 - 35] that the Raman signals of GeTe₄ and GaTe₄ tetrahedra overlap (at

least in glassy matrices, where bands are broad and more overlapping) – this is in general correspondence with the present results, as no new band (which already is not assigned to GeTe_4 vibrations) occurs with addition of Ga and also no large changes in mutual bands proportion occur as Ga is gradually added. Nonetheless, the spectra in Fig. 1B indicate (increases of the 140 cm^{-1} and 154 cm^{-1} peaks with GaTe_3 content) that presence of Ga leads to partial segregation of Te (larger signal corresponding to the Te chain backbone and Te dimers) and simultaneously possibly also to certain consolidation of the GeTe_4 network (higher signal of the edge-shared tetrahedra, which is however overlapped with that of Te chains). In addition, separated Te micro-regions are possibly formed within the amorphous Ge-Ga-Te structure. [36]

Micrographs in Figs. 1C and 1D show partially DSC-crystallized $(\text{GeTe}_4)_{60}(\text{GaTe}_3)_{40}$ and $(\text{GeTe}_4)_{86}(\text{GaTe}_3)_{14}$ bulk samples, respectively (the partial crystallinity was achieved non-isothermally at $5\text{ }^\circ\text{C}\cdot\text{min}^{-1}$). Clear distinction between the two crystal morphologies is apparent. At low GeTe_4 contents the initially formed crystallites tend to be spherical and the surface crystallization centres are fewer, in case of the high GeTe_4 contents the crystalline layer is very compact with no distinction between the particular crystallites (indicating extensive number of newly formed nuclei, i.e. true surface growth). The compositional borderline between the two cases is not very sharp and seems to be located at around 75 at.% GeTe_4 .

In order to identify the nature of the two gradually separating DSC peaks occurring at lower GeTe_4 contents, the XRD measurements were performed for all fully crystallized samples (Fig. 2) and for the two selected powder samples ($125 - 180\text{ }\mu\text{m}$, GeTe_4 contents of 40 and 50 at.%) heated in DSC only to the maximum of the first crystallization peak and then rapidly cooled (the diffraction patterns are included in Supplemental Online Material). The XRD patterns of fully crystallized samples show that all samples contain hexagonal Te

(P3121, 04-007-5290) and rhombohedral GeTe (R3m, 04-002-5568) – note that for the $(\text{GeTe}_4)_{40}(\text{GaTe}_3)_{60}$ material the GeTe diffraction lines are very weak but new (similarly weak) diffraction lines corresponding to the tetragonal Ga_2Te_5 (I/4m, 04-002-4771) occur. The third identified phase was the hexagonal Ga_2Te_5 (P3m1, 00-045-0954), however most of its strongest XRD lines fully overlap with those from Te. Based on the presence of several weaker Ga_2Te_5 lines (at 46, 49.5 and 67.9°) that are slightly shifted compared to the neighbouring Te lines, it can be concluded that the Ga_2Te_5 phase is present even for the $(\text{GeTe}_4)_{86}(\text{GaTe}_3)_{14}$ composition. Note that occurrence of the particular crystalline phases was independent from the powders size fraction (as tested for the finest and coarsest powders of compositions with 40, 67 and 100 at.% GeTe_4).

The XRD records obtained for the selected Ga-rich compositions heated up to the maximum of the first crystallization peak show that (apart from the Te phase) the Ga_2Te_5 phase is also present. This is quite unique as opposed to the iodine and selenium doped GeTe_4 matrices [21, 22, 37], where the Ge-Te-Se and Ge-I phases were formed during the second crystallization peak and only hexagonal Te was identified in the semi-crystalline product corresponding to the samples heated up to the first crystallization peak. In case of the present material the Ga_2Te_5 crystalline phase is formed from the primary nuclei simultaneously with hexagonal Te. This finding supports the conclusions derived in the structural study [32], i.e. that Ga atoms are not incorporated directly into the Ge-Te covalent network and bonded only to Te; hence the first Te precipitation initiates also the formation of Ga-Te crystalline phase. This is also supported by the IR micrographs in Figs. 1C and 1D, which depict the increased difficulty of the initial crystal formation (much lower number of primary nuclei and nucleation-growth mechanism as opposed to the pure surface growth) manifesting at higher Ga contents.

To understand the shift the second crystallization peak (corresponding mainly to rhombohedral GeTe) to higher temperatures with increased Ga content (see Fig. 1A), the overall influence of particle size on crystallization behavior needs to be considered. The data corresponding to the DSC measurements obtained at $10\text{ }^{\circ}\text{C}\cdot\text{min}^{-1}$ are for all studied $(\text{GeTe}_4)_x(\text{GaTe}_3)_{100-x}$ compositions and powder size fractions depicted in Figs. 3A, 3B and 3C. The following conclusions can be derived based on the DSC data:

- 1) the first crystallization peak shifts to significantly lower temperatures with decreasing particle size, which corresponds to the Te precipitation starting from surface and being catalyzed by presence of mechanically induced defects.
- 2) the onset of the first crystallization peak is almost invariant with regard to composition, which indicates that only low amount of Ga atoms is needed for the Te precipitation centers to be saturated (the onset of the first peak is not further influenced by increased presence of Ga atoms).
- 3) the higher the Ga content, the less the position of the second crystallization peak (presumably corresponding mainly to the formation of the GeTe phase) is influenced by particle size. This infers that at higher Ga contents the GeTe phase is formed in the volume of the grain, being not influenced by the rapidity of surface processes.
- 4) the stronger the Te precipitation (basically with decreasing powder size), the more prominent the separation of the two crystallization peaks with increasing Ga content. The formation of the GeTe phase being dependent on the preceding formation of the Te phase – compare the rapidity of the overall crystallization processes for pure GeTe_4 glass at different powder sizes (considering that incongruent crystal formation occurs – crystalline GeTe from base GeTe_4 matrix, depletion of Te from the base matrix due to its precipitation can initiate/accelerate formation of GeTe). The influence of gallium can

then be interpreted as not only stabilizing the remaining Ge-Te network but also preferentially occupying/utilizing the crystallization centers created by Te precipitation.

From the practical point of view, one of the most important features depicted in Figs. 3A-C is the marked invariance of the crystallization onset on composition. Apart from the pure GeTe₄ glass, the crystallization onsets for all other compositions with the given powder size are similar within ~ 3 – 5 °C. This is very important for the processing (drawing, moulding) and general stability of the studied glasses. Note that whereas it is usually the maximum of the crystallization peak that is used to evaluate the glass stability via e.g. the Hrubý criterion K_H (see Eq. 1), it is in fact the crystallization onset (temperature corresponding to the first occurrence of crystallites) that determines the true stability of the glass. The marked invariance of the crystallization onset with changing Ga content indicates that in case of the Ge-Ga-Te glasses the compositional evolution of glass stability will depend mostly on the position of T_g (due to the presence of eutectic, i.e. compositionally invariant T_m), the values of which were taken from [36], – as depicted in Fig. 3D. Consequently, it is the glasses with relatively low GaTe₃ content (15 – 20 at.%) that exhibit highest glass stability. The glass stability also naturally decreases with decreasing particle size due to the larger surface and higher amounts of mechanically induced defects that act as crystallization centers. Diminishing of this effect (as occurs at low GaTe₃ contents) is advantageous because of the correspondingly lower susceptibility of bulk glass towards undesirable crystal growth on various interfaces and/or microscopic bruises. Based on the above-described findings, the (GeTe₄)₈₆(GaTe₃)₁₄ composition appears to be most suitable for far-IR applications utilizing fully glassy materials.

$$K_H = (T_c - T_g) / (T_m - T_c) \quad (1)$$

In order to describe the DSC crystallization data, a series of 6 measurements at different heating rates was performed for each composition and powder size; example of such

dataset is for the 300–500 μm $(\text{GeTe}_4)_{50}(\text{GaTe}_3)_{50}$ powder shown in Fig. 3E. Each dataset was then evaluated by means of multivariate kinetic analysis MKA [38], a nonlinear optimization method based on the following set of equations, including the standard DSC equation (Eq. 4):

$$RSS = \sum_{j=1}^n \sum_{k=First_j}^{Last_j} w_{j,k} (\Phi_{exp_{j,k}} - \Phi_{cal_{j,k}})^2 \quad (2)$$

$$w_{j,k} = \frac{\sum_{i=1}^n (Last_i - First_i)}{n(Last_j - First_j) [abs(Max(Y_{exp_{j,k}})) + abs(Min(Y_{exp_{j,k}}))]} \quad (3)$$

$$\Phi = \Delta H \cdot A \cdot e^{-E/RT} \cdot f(\alpha) \quad (4)$$

where RSS is the sum of squared residua, n is number of measurements, j is index of the given measurement, $First_j$ is the index of the first point of the given curve, $Last_j$ is the index of the last point of the given curve, $Y_{exp_{j,k}}$ is the experimental value of the point k of curve j , $Y_{cal_{j,k}}$ is the calculated value of the point k of curve j , $w_{j,k}$ is weighting factor for the point k of curve j , Φ is the measured heat flow, ΔH is the crystallization enthalpy, A is the pre-exponential factor, E is the apparent activation energy of the process, R is the universal gas constant, T is temperature and $f(\alpha)$ stands for an expression of a kinetic model with α being conversion. Note that the expression for $w_{j,k}$ (Eq. 3) is optimized for the DSC measurements, so that each measured curve is weighted despite the different number of measured points and increased errors due to the magnifying influence of heating rate on measured heat flow.

During the MKA optimization the standard available 21 kinetic models and their mutual dependences (different reaction routes involving the parallel, competing, consecutive, independent, switching, reversible reaction, independent inhibition and by-product inhibition reaction mechanisms) were tested. Based on the best correlation coefficient the combination of two independent crystallization sub-processes following the nucleation-growth Johnson-Mehl-Avrami [39 - 42] (JMA, the low-temperature one) and the autocatalytic Šesták-

Berggren [43] (AC, the high-temperature one) kinetics. The JMA and AC models are expressed by the following equations, respectively:

$$f(\alpha) = m(1-\alpha)[- \ln(1-\alpha)]^{1-(1/m)} \quad (5)$$

$$f(\alpha) = \alpha^M (1-\alpha)^N \quad (6)$$

where m , M and N are the kinetic parameters of the two models. Example of such kinetic deconvolution of the complex crystallization process is shown in Fig. 3F.

Multivariate kinetic analysis provided complete enumeration of Eq. 4 for each measured dataset. Graphs in Fig. 4 depict the obtained compositional and powder size dependences of the overall and particular crystallization enthalpies. The compositionally invariant overall crystallization enthalpy (approx. $40 \text{ J}\cdot\text{g}^{-1}$) suggests that formation of both major crystalline phases (Ga_2Te_5 and GeTe) manifest with roughly similar evolved heat. This definitely means that the increased crystallization enthalpy obtained for the first crystallization peak at high GaTe_3 contents (see Fig. 4C) has to be associated with formation of the additional GaTe_3 phase because the amount of surplus Te decreases with decreasing GeTe_4 content (note that GeTe_4 composition can crystallize into rhombohedral GeTe and three times the amount of hexagonal Te; i.e. the amount of crystalline Te and hence the enthalpy of the first crystallization peak should decrease if only the tellurium phase was formed during that process). This effect is more pronounced for fine powders, thus also the formation of the GaTe_3 crystallites is accelerated by increased presence of mechanically induced defects. Accordingly, the crystallization enthalpy associated with the second crystallization peak decreases for fine powders as the amount of available GeTe_4 phase decreases. Interestingly, for coarse powder fraction (with large bulk-to-surface ratio) the crystallization enthalpy of the second crystallization peak does not change, which indicates that formation of the GaTe_3 crystalline phase is largely enhanced by the presence of mechanically induced defects and their absence leads to the GaTe_3 phase formation being

relocated towards the secondary crystal growth initiated together with the formation of the GeTe phase.

Apart from determination of the crystallization enthalpy, the MKA method provided full set of kinetic parameters for each measured dataset. In Fig. 5A the apparent activation energy of the crystallization process is shown for the two sub-processes in dependence on composition and particle size. The E values are generally slightly lower for the second sub-process; the larger the difference the more the crystallization of the system is controllable via application of different heating rate, which may be advantageous through enlarged portfolio of controlled crystal growth options in glass-ceramics applications. On the other hand, for applications requiring fully ceramic material the consistency of crystal formation is needed, prioritizing the simultaneous formation of all crystalline phases, as found for coarse powders with low GaTe₃ content. These powders exhibit larger difference in activation energies of the two crystallization sub-processes (which in theory should be disadvantageous for controlled preparation of ceramics), however considering that only a limited range of heating rates is usually applied for the ceramics processing, the difference in E values should not be an issue.

The kinetic parameters of the JMA and AC models determined by MKA for all studied datasets are depicted in Fig. 5B. Most trends in the compositional/powder size evolution of the parameters are rather uniform and well identifiable, ensuring reliable crystal growth prediction for the potential glass-ceramics applications. Similar conclusion arises also from the relatively high correlation coefficients (see Fig. 5C), indicating not only high reliability of the data but also their consistency with respect to the applied heating rate (note that in MKA a simultaneous optimization of all six measurements obtained at different q^+ was applied). To further explore the possible restrictions arising from q^+ slightly influencing the shape of the kinetic peaks and thus the resulting kinetic parameters, the modified MKA was applied, based on individual optimization for each DSC curve employing fixed E values (determined during

the simultaneous fit). The values of kinetic parameters obtained for different q^+ were then used to predict the rate of crystalline phase formation at intermediate heating rate to demonstrate the effects of averaging and extrapolations on the kinetic prediction. This is for the 125 – 180 μm $(\text{GeTe}_4)_{50}(\text{GaTe}_3)_{50}$ powder (where the differences in parameters were largest) demonstrated in Fig. 5D. As is apparent, the averagings/extrapolations have only very small effect on kinetic predictions (confirming the relatively good consistency of the data with respect to q^+) and thus can be for the present materials neglected in the glass-ceramics development.

4. Conclusions

The crystallization behavior of the $(\text{GeTe}_4)_x(\text{GaTe}_3)_{100-x}$ glasses was studied by means of DSC, XRD infrared microscopy and Raman spectroscopy. The study was performed in dependence on particle size to demonstrate the influence of the mechanically induced defects and increased surface on the crystal growth tendency. The complex crystallization data consisting of two main overlapping peaks were deconvoluted by means of multivariate kinetic analysis and the following crystal growth mechanisms were identified: the crystallization starts with the precipitation of hexagonal tellurium and formation of hexagonal Ga_2Te_5 phase (following the nucleation-growth JMA kinetics); the second crystallization peak then corresponds to formation of the rhombohedral GeTe and remaining Ga_2Te_5 phases, which follow the autocatalytic kinetics. The initial crystallization peak increased in magnitude with increase of GaTe_3 content and with decrease of powder particle size, indicating that presence of mechanically induced defects enhances formation of the GaTe_3 crystallites. Based on the glass stability criteria (evaluated for the crystallization onsets for better accuracy), the $(\text{GeTe}_4)_{86}(\text{GaTe}_3)_{14}$ composition appears to be most stable and indifferent to the presence of structural/morphological defects, and hence most suitable for far-IR applications utilizing

fully glassy materials. Regarding the $(\text{GeTe}_4)_x(\text{GaTe}_3)_{100-x}$ ceramics, the glasses with low GaTe_3 content seem to be most suitable here, too, due to the simultaneous formation of all crystalline phases invariant with applied experimental conditions. On the other hand, for the case of the glass-ceramics processing the materials with high GaTe_3 content exhibit the most uniform crystallization behaviour, offering the best control over the crystal growth process. Crystal growth predictions utilizing the q^+ -dependent kinetic parameters have shown that the effect of heating rate dependent kinetics is negligible for the Ge-Ga-Te glasses and does not have to be considered for the processing of the corresponding ceramics.

Acknowledgements

This work has been supported by the Czech Science Foundation under project No. 17-11753S.

References

- [1] B. Bureau, S. Danto, H.L. Ma, C. Boussard-Plédel, X.H. Zhang, J. Lucas. Tellurium based glasses: A ruthless glass to crystal competition. *Solid State Sci.* 10 (2008) 427-33.
- [2] S. Cui, R. Chahal, C. Boussard-Plédel, V. Nazabal, J.L. Doualan, J. Troles, J. Lucas, B. Bureau, From selenium- to tellurium-based glass optical fibers for infrared spectroscopies, *Molecules* 18 (2013) 5373-5388.
- [3] A.A. Wilhelm, C. Boussard-Plédel, Q. Coulombier, J. Lucas, B. Bureau, P. Lucas. Development of far-infrared-transmitting te based glasses suitable for carbon dioxide detection and space optics. *Adv. Mater.* 19 (2007) 3796–3800.
- [4] B. Bureau, C. Boussard-Plédel, P. Lucas, X. Zhang, J. Lucas. Forming glasses from Se and Te. *Molecules* 14 (2009) 4337–50.
- [5] R. Svoboda, D. Brandová, J. Málek. Non-isothermal crystallization kinetics of GeTe_4 infrared glass. *J. Therm. Anal. Calorim.* 123 (2016) 195-204.
- [6] S. Danto, P. Houizot, C. Boussard-Plédel, X.H. Zhang, F. Smektala, J. Lucas. A family of far-infrared-transmitting glasses in the Ga-Ge-Te system for space applications. *Adv. Funct. Mater.* 16 (2006) 1847-52.
- [7] G. Wang, Q. Nie, X. Wang, S. Dai, T. Xu, X. Shen, X. Zhang, Composition dependence of optical band gap of the Se–Ge–Te far infrared transmitting glasses, *Physica B* 405 (2010) 4424-4428.
- [8] C. Conseil, V.S. Shiryaev, S. Cui, C. Boussard-Plédel, J. Troles, A.P. Velmuzhov, A.M. Potapov, A.I. Suchkov, M.F. Churbanov, B. Bureau, Preparation of High Purity Te-Rich Ge-Te-Se Fibers for 5–15 m Infrared Range. *J. Lightwave Technol.* 31 (2013) 1703-1707.

- [9] C. Cheng, X. Wang, T. Xu, M. Zhu, Ch. Jiang, Q. Zhu, F. Liao, Q. Nie, S. Dai, X. Shen, P. Zhang, X. Zhang. Research on preparation and optical properties of far infrared Ge-Te-I chalcogenide glasses with halogen. *Guangzi Xuebao/Acta Photonica Sinica* 44 (2015) 0216002.
- [10] G. Wang, Q. Nie, M. Barj, X. Wang, S. Dai, X. Shen, T. Xu, X. Zhang. Compositional dependence of the optical properties of nvel Ge-Ga-Te-CsI far infrared transmitting chalcogenide glasses system. *J. Phys. Chem. Sol.* 72 (2011) 5-9.
- [11] P. Petkov, V. Ilcheva, D. Wamwangi, M. Wuttig, P. Ilchev, T. Petkova. Phase transition of gallium containing telluride thin films. *J. Optoelectron. Adv. M.* 11 (2009) 1261-4.
- [12] Q. Nie, G. Wang, X. Wang, S. Dai, S. Deng, T. Xu, X. Shen. Glass formation and properties of GeTe₄-Ga₂Te₃-AgX (X=I/Br/Cl) far infrared transmitting chalcogenide glasses. *Optics Communications* 283 (2010) 4004-7.
- [13] G. Tao, H. Ebendorff-Heidepriem, A.M. Stolyarov, S. Danto, J.V. Badding, Y. Fink, J. Ballato, A.F. Abouraddy. Infrared fibers. *Adv. Opt. Photonics* 7 (2015) 379-458.
- [14] X.H. Zhang, L. Calvez, V. Seznec, H.L. Ma, S. Danto, P. Houizot, C. Boussard-Plédel, J. Lucas. Infrared transmitting glasses and glass-ceramics. *J. Non-Cryst. Sol.* 352 (2006) 2411-5.
- [15] C. Lin, C. Russel, S. Dai. Chalcogenide glass-ceramics: Functional design and crystallization mechanism. *Prog. Mater. Sci.* 93, 1 – 44 (2018).
- [16] B. Karmakar. Functional chalcogenide glasses and glass-ceramics. In: *Functional glasses and glass-ceramics*, ed. B. Karmakar, Elsevier, 2017.
- [17] L. Calvez. Chalcogenide glasses and glass-ceramics: Transparent materials in the infrared for dual applications. *Compt. Rend. Phys.* 18, 5_6, 314 – 322 (2017).
- [18] L. Calvez. Transparent chalcogenide glass-ceramics. In: *Chalcogenide glasses*, eds. J.L. Adam, X. Zhang, Woodhead Publishing (2014).
- [19] M. Hubert, L. Calvez, X. Zhang, P. Lucas. Enhanced luminescence in Er³⁺-doped chalcogenide glass-ceramics based on selenium. *Opt. Mater.* 35, 12, 2527 – 2530 (2013).
- [20] M. Hubert, E. Petracovschi, X. Zhang, L. Calvez. Synthesis of germanium-gallium-tellurium (Ge-Ga-Te) ceramics by ball-milling and sintering. *J. Am. Ceram. Soc.* 96, 5, 1444 – 1449 (2013).
- [21] R. Svoboda, D. Brandová, M. Chromčíková, M. Setnička, J. Chovanec, A. Černá, M. Liška, J. Málek. Se-doped GeTe₄ glasses for far-infrared optical fibers. *J. Alloys Compd.* 695 (2017) 2434 - 2443
- [22] R. Svoboda, D. Brandová, J. Málek. Thermal behavior of Ge₂₀Se_yTe_{80-y} infrared glasses (for y up to 8 at.%). *J. Alloys Compd.* 680 (2016) 427-435.
- [23] D. Brandová, R. Svoboda, J. Málek. Influence of particle size on crystallization and relaxation behavior of Ge₂₀Se₄Te₇₆ glass for infrared optics. *J. Non-Cryst. Sol.* 433 (2016) 75-81.
- [24] R. De Bastiani, E. Carria, S. Gibilisco, M.G. Grimaldi, A.R. Pennisi, A. Gotti, A. Pirovano, R. Bez, E. Rimini. Ion-irradiation-induced selective bond rearrangements in amorphous GeTe thin films. *Phys. Rev. B* 80 (2009) 245205
- [25] K.S. Andrikopoulos, S.N. Yannopoulos, G.A. Voyiatzis, A.V. Kolobov, M. Ribes, J. Tominaga. Raman scattering study of the a-GeTe structure and possible mechanism for the amorphous-to-crystal transition. *J. Phys. Condens. Matter* 18 (2006) 965-979.
- [26] M. Upadhyay, S. Murugavel, M. Anbarasu, T.R. Ravindran. Structural study on amorphous and crystalline state of phase change material. *J. Appl. Phys.* 110 (2011) 083711

- [27] S.S. Garje, M.C. Copsey, M. Afzaal, P.O. Brian, T. Chivers. Aerosol-assisted chemical vapour deposition of indium telluride thin films from $\{\text{In}(\mu\text{-Te})[\text{N}(\text{Pr}_2\text{PTE})_2]\}_3$. *J. Mater. Chem.* 16 (2006) 4542-4547.
- [28] O. Uemura, N. Hayasaka, S. Tokairin, T. Usuki. Local atomic arrangement in Ge-Te and Ge-S-Te glasses. *J. Non-Cryst. Solids* 205 (1996) 189-193.
- [29] A.S. Pine, G. Dresselhaus. Raman Spectra and Lattice Dynamics of Tellurium. *Phys. Rev. B* 4 (1971) 356.
- [30] Y.M. Azhniuk, Y.I. Hutykh, V.V. Lopushansky, M.V. Prymak, A.V. Gomonnai, D.R.T. Zahn. Raman Spectra of Quaternary $\text{CdS}_{1-x-y}\text{Se}_x\text{Te}_y$ Nanocrystals Embedded in Borosilicate Glass. *Inter. J. Spec.* 2012 (2012) 495896
- [31] M.H. Brodsky, R.J. Gambino, J.E. Smith, Y. Yacoby. The Raman Spectrum of Amorphous Tellurium. *Phys. Status Solidi B* 52 (1972) 609-614.
- [32] P. Jovari, I. Kaban, B. Bureau, A. Wilhelm, P. Lucas, B. Beuneu, D.A. Zajac. Structure of Te-rich Te-Ge-X (X = I, Se, Ga) glasses. *J. Phys.: Condens. Matter* 22 (2010) 404207.
- [33] I. Voleská, J. Akola, P. Jovari, J. Gutwirth, T. Wágner, Th. Vasileiadis, S.N. Yannopoulos, R.O. Jones. Structure, electronic, and vibrational properties of glassy $\text{Ga}_{11}\text{Ge}_{11}\text{Te}_{78}$: Experimentally constrained density functional study. *Phys. Rev. B* 86 (2012) 094108.
- [34] S. Sen, E.L. Gjersing, B.G. Aitken. Physical properties of $\text{Ge}_x\text{As}_{2x}\text{Te}_{100-3x}$ glasses and Raman spectroscopic analysis of their short-range structure. *J. Non-Cryst. Solids* 356 (2010) 2083-2088.
- [35] P. Němec, V. Nazabal, M. Dussauze, H.-L. Ma, Y. Bouyrie, X.-H. Zhang. Ga-Ge-Te amorphous thin films fabricated by pulsed laser deposition. *Thin Solid Films* 531 (2013) 454-459.
- [36] R. Svoboda, M. Setnička, Z. Zmrhalová, D. Brandová, J. Málek. Structural interpretation of the enthalpy relaxation kinetics of $(\text{GeTe}_4)_y(\text{GaTe}_3)_{1-y}$ far-infrared glasses. *J. Non-Cryst. Sol.* 447 (2016) 110-116.
- [37] D. Brandová – personal communication regarding unpublished results on Ge-Te-I chalcogenide system.
- [38] J. Opfermann. Kinetic analysis using multivariate non-linear regression. *J. Therm. Anal. Calorim.* 60 (2000) 641-58.
- [39] M. Avrami. Kinetics of phase change I – General theory. *J. Chem. Phys.* 7 (1939) 1103–12.
- [40] M. Avrami. Kinetics of phase change. II – Transformation-time relations for random distribution of nuclei. *J Chem Phys.* 7 (1940) 212–24.
- [41] M. Avrami. Granulation, phase change, and microstructure – kinetics of phase change III. *J Chem Phys.* 7 (1941) 177–84.
- [42] W.A. Johnson, K.F. Mehl. Reaction kinetics in processes of nucleation and growth. *Trans. Am. Inst. Min. (Metall) Eng.* 135 (1939) 416–42.
- [43] J. Šesták. *Thermophysical Properties of Solids, Their Measurements and Theoretical Analysis.* Elsevier: Amsterdam; 1984.

Figure captions

Fig. 1: A) Example DSC curves obtained for the 125 – 180 μm powders heated at $1\text{ }^\circ\text{C}\cdot\text{min}^{-1}$ and all studied $(\text{GeTe}_4)_x(\text{GaTe}_3)_{100-x}$ compositions. Exothermic effects evolve in the upwards direction.

B) Raman spectra obtained for all studied $(\text{GeTe}_4)_x(\text{GaTe}_3)_{100-x}$ compositions.

C) Infrared micrograph for the partially crystalline $(\text{GeTe}_4)_{60}(\text{GaTe}_3)_{40}$ bulk sample.

D) Infrared micrograph for the partially crystalline $(\text{GeTe}_4)_{86}(\text{GaTe}_3)_{14}$ bulk sample.

Fig. 2: Diffraction patterns of fully DSC-crystallized $(\text{GeTe}_4)_x(\text{GaTe}_3)_{100-x}$ materials.

Fig. 3: A) DSC crystallization data obtained for 20 – 50 μm powders heated at $10\text{ }^\circ\text{C}\cdot\text{min}^{-1}$.

B) DSC crystallization data obtained for 125 – 180 μm powders heated at $10\text{ }^\circ\text{C}\cdot\text{min}^{-1}$.

C) DSC crystallization data obtained for 300 – 500 μm powders heated at $10\text{ }^\circ\text{C}\cdot\text{min}^{-1}$.

D) Compositional dependences of glass transition temperatures (obtained at $10\text{ }^\circ\text{C}\cdot\text{min}^{-1}$) and Hrubý criteria (evaluated from crystallization onsets and in dependence on particle size).

E) Example kinetic dataset (set of DSC crystallization curves obtained at different q^+) obtained for the 300–500 μm $(\text{GeTe}_4)_{50}(\text{GaTe}_3)_{50}$ powder.

F) Example MKA deconvolution of the $20\text{ }^\circ\text{C}\cdot\text{min}^{-1}$ DSC curve from graph E.

Fig. 4: Compositional and particle size dependences of the overall (ΔH) and particular (ΔH_1 , ΔH_2) crystallization enthalpies determined via MKA.

Fig. 5: Compositional and particle size dependences of apparent activation energies (graph A), JMA and AC kinetic exponents (graph B) and correlation coefficients (graph C) obtained from MKA. Graph D depicts theoretically simulated data for $q^+ = 5\text{ }^\circ\text{C}\cdot\text{min}^{-1}$, where the kinetic parameters were obtained by the modified single-curve-optimized MKA (for the DSC curves measured at 1, 5, 10 and $30\text{ }^\circ\text{C}\cdot\text{min}^{-1}$) with fixed E values (obtained from the simultaneous optimization of all DSC curves).

Fig 1

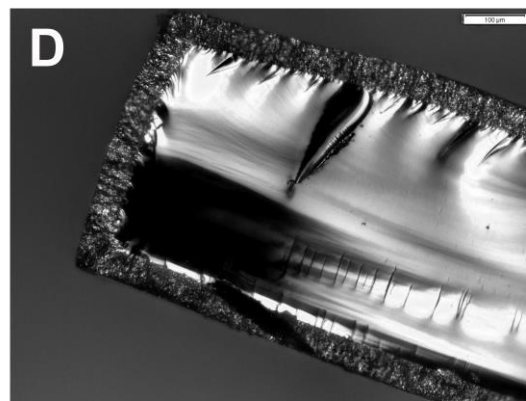
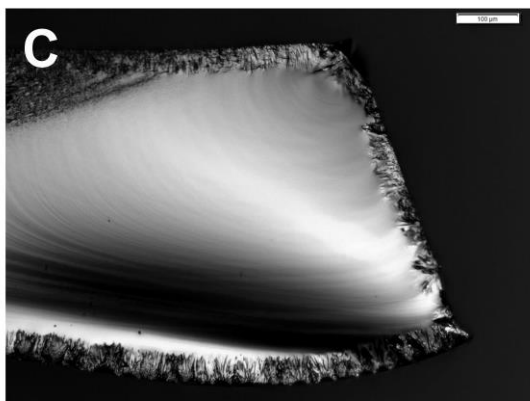
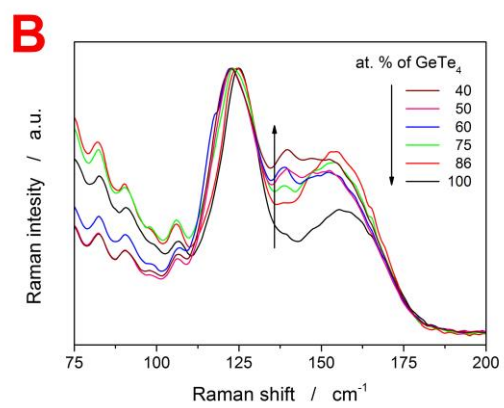
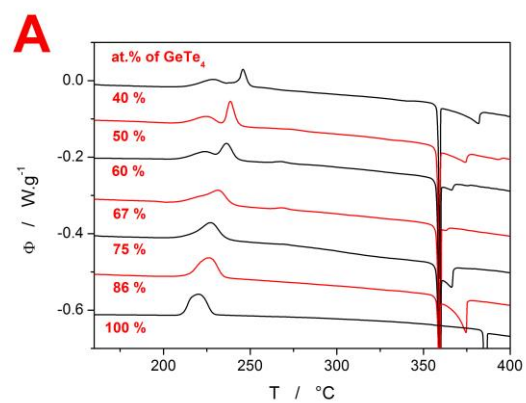


Fig 2

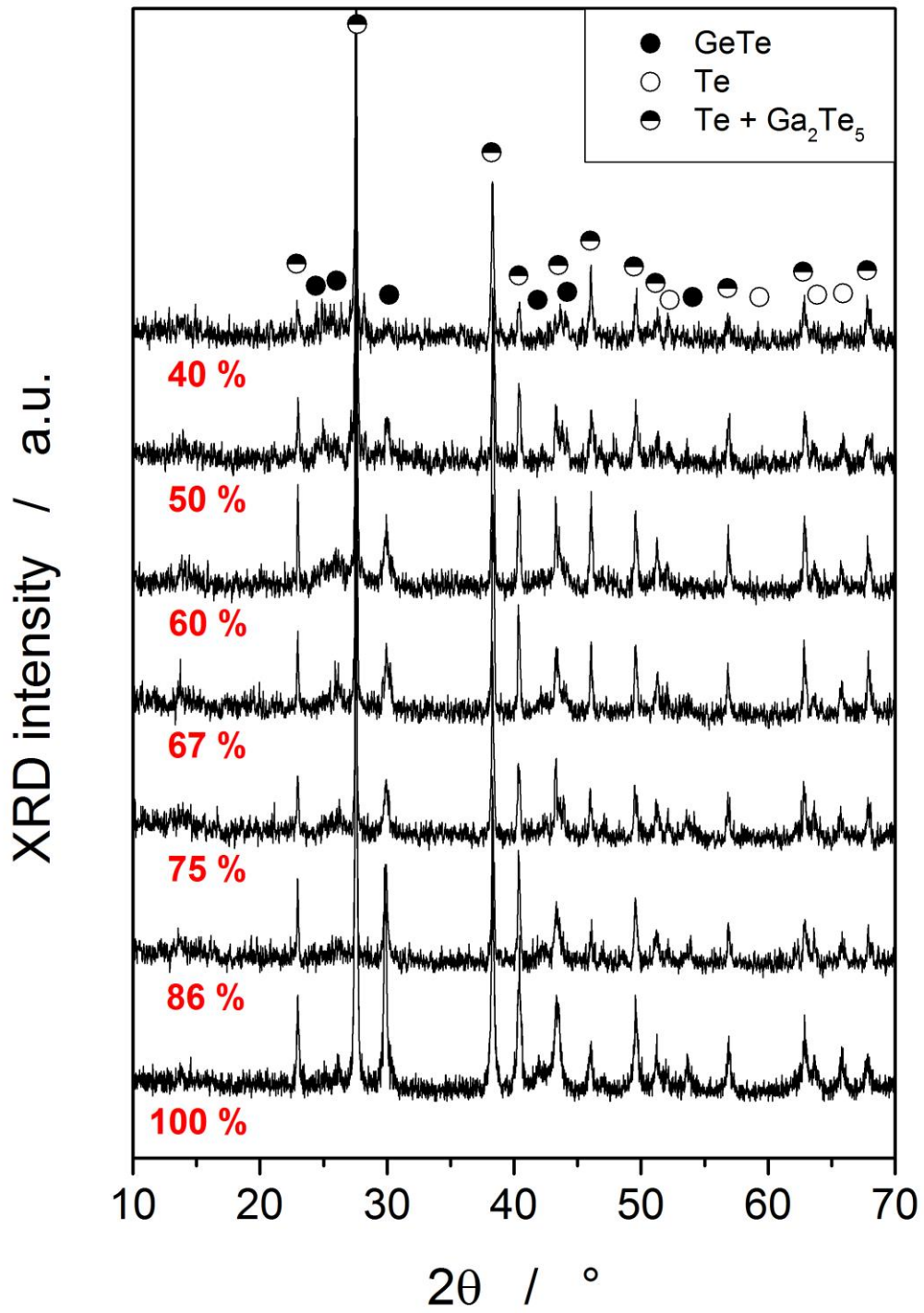


Fig 3

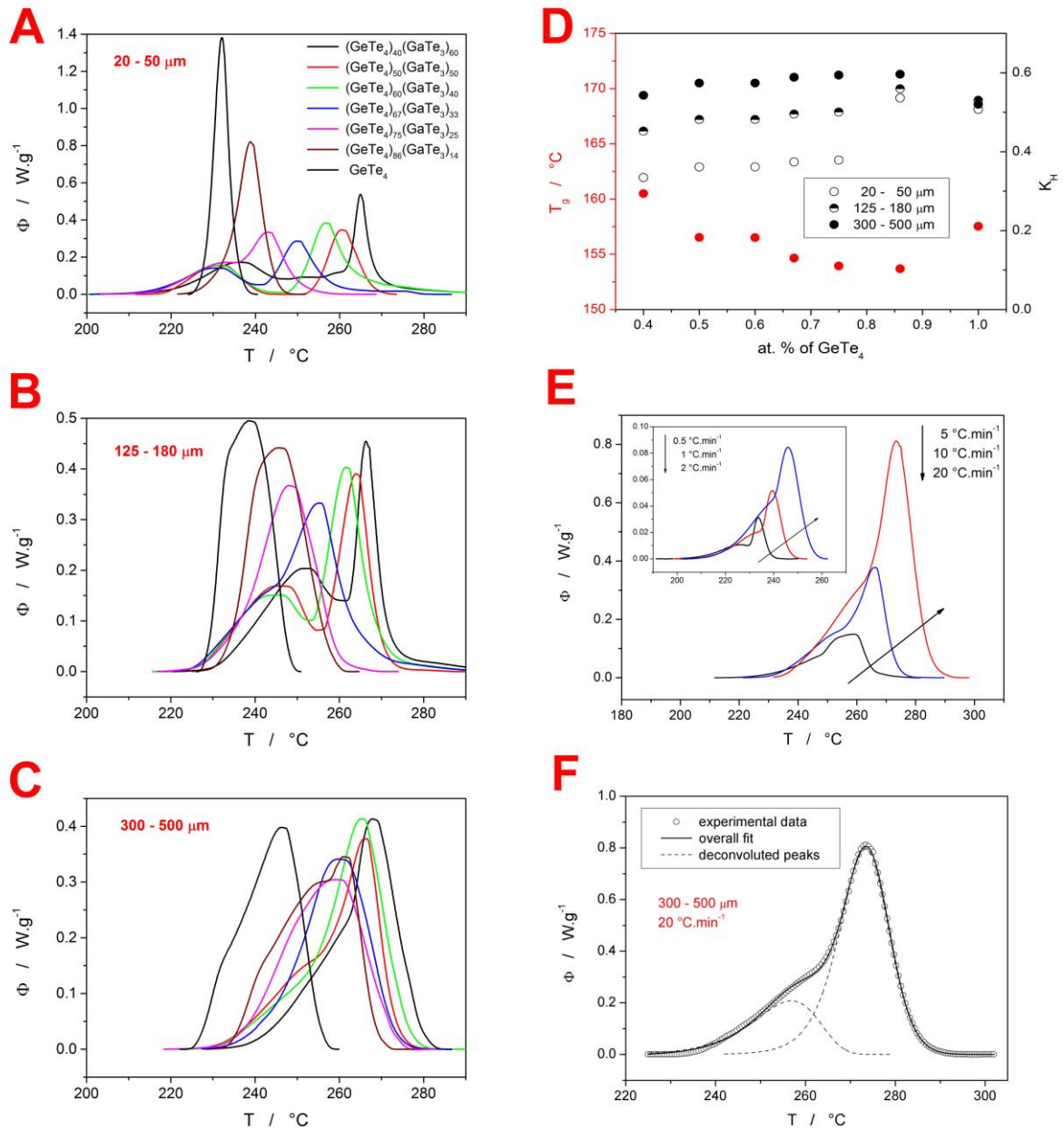


Fig 4

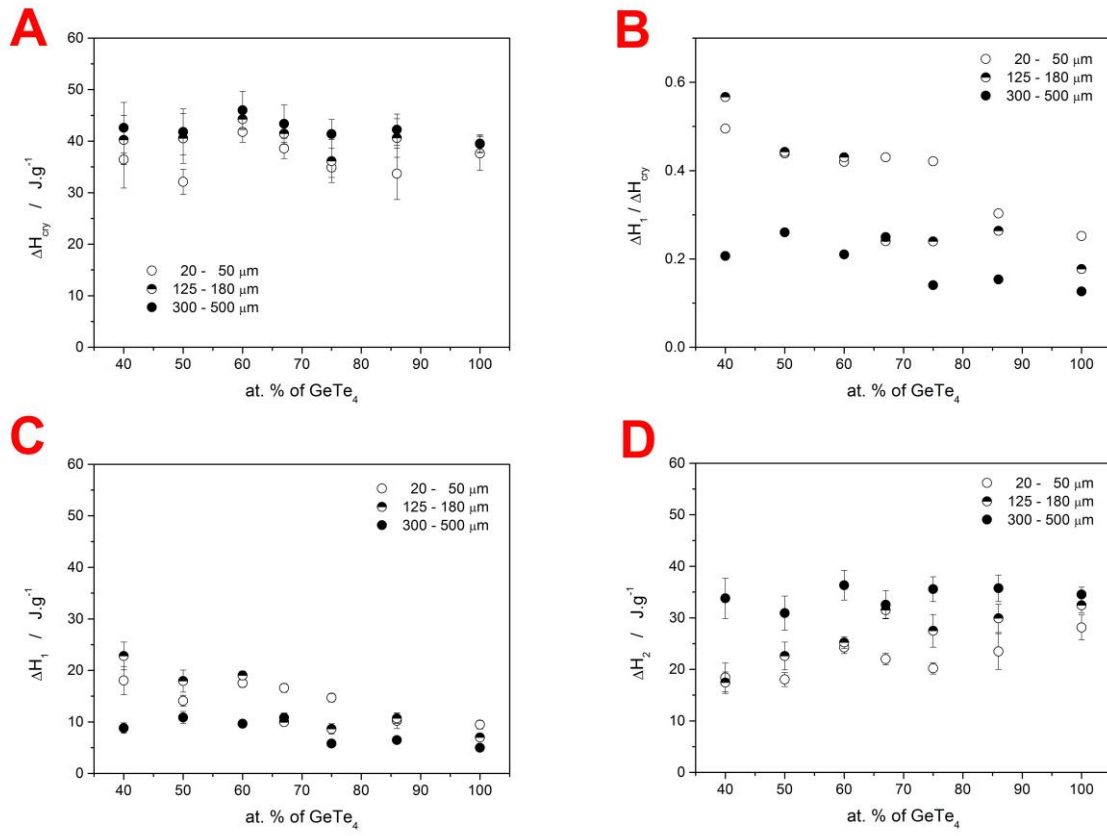


Fig 5

